processes

MDPI

Article

Ultrasonic Vibration-Assisted CNC Milling of 90CrSi Steel Cylindrical Surfaces: Horn Design, Experimental Analysis, and Multi-Objective Optimization

Huu-Danh Tran [1], Thu-Quy Le [2], Ngoc-Pi Vu [3] and Thanh-Cuong Pham [3,*]

[1] Faculty of Mechanical Engineering, Vinh Long University of Technology Education, 73 Nguyen Hue Street, Long Chau Ward, Vinh Long 85000, Vietnam; danhth@vlute.edu.vn
[2] National Research Institute of Mechanical Engineering, 04 Pham Van Dong, Hanoi 11309, Vietnam; quylt@narime.gov.vn
[3] Faculty of Mechanical Engineering, Thai Nguyen University of Technology, 3/2 Street, Tich Luong Ward, Thai Nguyen 24000, Vietnam; vungocpi@tnut.edu.vn
* Correspondence: phamcuong@tnut.edu.vn

Abstract

This study investigates ultrasonic vibration-assisted (UV) CNC milling of hardened 90CrSi steel cylindrical surfaces, with emphasis on ultrasonic horn design, experimental analysis, and multi-objective optimization of machining parameters, addressing the need for an integrated framework combining system design, experimental validation, and multi-objective optimization. A quarter-wavelength ultrasonic horn was designed and experimentally validated to operate at a frequency of 20 kHz. By adjusting the horn–workpiece system, stable vibration amplitudes were achieved to enable effective ultrasonic-assisted milling of cylindrical surfaces. Milling experiments based on a Box–Behnken design were conducted to examine the effects of vibration amplitude, cutting speed, feed rate, and radial depth of cut on material removal rate (MRR) and surface roughness (Ra). Surrogate models using response surface methodology (RSM) and Gaussian process regression (GPR) were developed to predict machining performance. A GPR-assisted NSGA-II algorithm was then applied to simultaneously maximize MRR and minimize Ra, resulting in a well-defined Pareto front that reveals the trade-off between machining productivity and surface quality. Furthermore, an AHP-based decision-making approach was employed to select preferred machining conditions from the Pareto-optimal solutions. The GPR models demonstrated high predictive accuracy ($R^2 > 0.98$), and validation experiments confirmed the reliability of the predicted optimal results, with deviations below 5%. In addition, a comparative analysis between ultrasonic-assisted and conventional milling showed that MRR increased by 10.81–40.17%, Ra decreased by 27.11–44.44%, and cutting force was reduced by 14.2–42.65%, providing direct experimental evidence of improved machinability. The results demonstrate that the proposed integrated framework provides an effective strategy for optimizing ultrasonic vibration-assisted milling processes and improving the machinability of hardened 90CrSi cylindrical surfaces. Overall, the proposed framework provides a practical and cost-effective strategy for enhancing machining performance and offers a robust approach for multi-objective optimization of ultrasonic vibration-assisted milling processes.

Keywords: ultrasonic vibration-assisted milling; cylindrical surface machining; 90CrSi alloy steel; material removal rate; surface roughness

Academic Editors: Constantin Alberto Hernández Bocanegra, José Ángel Ramos-Banderas and Gildardo Solorio Diaz

Received: 18 March 2026
Revised: 17 April 2026
Accepted: 25 April 2026
Published: 30 April 2026

Processes **2026**, *14*, 1451 https://doi.org/10.3390/pr14091451

1. Introduction

Hard-to-machine materials such as high-strength steels, superalloys, and particle-reinforced composites are widely used in modern engineering applications due to their superior mechanical properties, wear resistance, and thermal stability. However, these characteristics also lead to significant challenges in conventional milling processes, including high cutting forces, rapid tool wear, elevated cutting temperatures, and poor surface integrity. As a result, advanced machining technologies have been actively developed to enhance machining efficiency and surface quality.

Among these technologies, ultrasonic vibration-assisted machining (UVAM) has emerged as a promising approach. By superimposing high-frequency vibration onto the cutting motion, ultrasonic-assisted milling introduces an intermittent cutting mechanism that reduces tool–workpiece contact time, improves chip evacuation, and lowers cutting forces. Numerous recent studies have demonstrated the effectiveness of ultrasonic vibration in improving machining performance across various materials. For instance, ultrasonic vibration-assisted milling has been shown to significantly enhance surface quality and reduce cutting forces in composite materials and biological structures [1–3]. Similar improvements have been reported for metal matrix composites and advanced alloys, where ultrasonic vibration contributes to improved material removal mechanisms and surface integrity [4–6].

In addition to experimental studies, considerable efforts have been devoted to modeling and prediction of machining behavior under ultrasonic vibration. Various analytical, numerical, and machine learning approaches have been proposed to predict cutting forces, temperature distribution, and surface characteristics [7–9]. Furthermore, hybrid machining processes combining ultrasonic vibration with laser or electrical discharge assistance have demonstrated enhanced machining performance for difficult-to-cut materials such as Inconel 718 and cemented carbides [9–11]. These studies confirm that ultrasonic vibration plays a critical role in improving both machinability and process stability.

From a broader perspective, ultrasonic vibration-assisted milling has been successfully applied to a wide range of materials, including nickel-based superalloys, titanium alloys, and ceramic composites. Improvements in tool wear resistance, surface integrity, and fatigue performance have been widely reported [12–15]. In addition, ultrasonic vibration has been shown to enhance tribological properties and reduce friction during machining, further contributing to improved surface quality [16]. These benefits highlight the potential of ultrasonic-assisted milling as an effective solution for machining advanced engineering materials.

Despite these advances, most existing studies focus on configurations in which ultrasonic vibration is applied directly to the cutting tool. In contrast, relatively limited research has investigated systems where ultrasonic vibration is transmitted directly to the workpiece, particularly along the axial direction during milling operations. Such configurations may offer advantages in terms of vibration transmission efficiency, structural simplicity, and improved control of vibration amplitude at the machining interface.

Another important aspect of ultrasonic machining systems is the design of the ultrasonic horn, which is responsible for amplifying vibration amplitude and transmitting ultrasonic energy from the transducer to the machining zone. The horn geometry, resonant length, and material properties significantly influence vibration efficiency and system stability. However, only a few studies have systematically integrated horn design with experimental machining analysis and optimization of process parameters within a unified framework.

In practical manufacturing, many industrial components contain profiled cylindrical surfaces, such as punches used in sheet-metal forming and tablet compression tools in pharmaceutical production (Figure 1). These components are typically made of hardened tool steels, such as 90CrSi, which are difficult to machine using conventional methods. Achieving both high productivity and good surface quality in machining such cylindrical surfaces remains a significant challenge.

Figure 1. Tablet compression punches used in pharmaceutical manufacturing, representing typical components with profiled cylindrical surfaces.

Recently, advanced machining methods assisted by ultrasonic vibration have been explored for processing external cylindrical surfaces. In particular, ultrasonic vibration-assisted electrical discharge machining (UV-EDM), where electrical discharges are combined with high-frequency vibration, has been applied to cylindrical surface machining and shown promising potential in improving material removal and surface characteristics [17]. In addition, ultrasonic vibration-assisted CBN grinding of external cylindrical surfaces has been investigated using multi-objective optimization approaches to simultaneously enhance surface quality and material removal rate [18]. These studies demonstrate that ultrasonic-assisted machining is increasingly being extended to cylindrical geometries across both non-traditional and abrasive machining processes. However, systematic investigations on ultrasonic vibration-assisted milling of hardened cylindrical surfaces, especially integrating horn design, experimental analysis, and multi-objective optimization, remain limited. Despite these advances, several important limitations persist in the current literature. First, most existing UVAM studies apply ultrasonic vibration to the cutting tool, resulting in complex and costly system configurations that require specialized rotating ultrasonic tool holders and spindle-integrated devices. Second, limited attention has been given to workpiece-based vibration systems, particularly for cylindrical surface machining of hardened steels. Third, surrogate-based optimization approaches are often developed independently of the physical design of the ultrasonic system, with little consideration of horn–workpiece resonance characteristics and amplitude controllability. These limitations highlight the need for a unified and practically implementable framework that integrates system design, experimental investigation, and optimization.

To address these issues, the present study investigates ultrasonic vibration-assisted CNC milling of hardened 90CrSi cylindrical surfaces using a nano-composite coated tool. In contrast to conventional tool-based approaches, ultrasonic vibration is transmitted directly to the workpiece through a specially designed horn, which not only enhances vibration transmission efficiency for cylindrical surface machining but also significantly reduces system cost and complexity by eliminating the need for expensive rotating ultrasonic tool holders. A quarter-wavelength ultrasonic horn is designed and experimentally validated to ensure effective transmission of longitudinal vibration to the workpiece. Milling experiments based on a Box–Behnken design are conducted to evaluate the influence of machining parameters on material removal rate and surface roughness. Subsequently, surrogate models are developed and integrated with a multi-objective optimization framework based on NSGA-II to simultaneously maximize MRR and minimize Ra. Finally, an AHP-based decision-making approach is employed to select preferred machining conditions from the Pareto-optimal solutions.

Therefore, the main contribution of this study lies not only in the application of surrogate-assisted multi-objective optimization, but more importantly in the development of a cost-effective workpiece-vibration UVAM configuration and its integration with horn–workpiece system design, amplitude control via workpiece length calibration, and multi-objective decision-making within a unified framework. This approach advances current UVAM research by explicitly linking system-level design with process optimization for cylindrical surface machining of hardened steels, thereby providing both new scientific insights and a practical pathway toward industrial implementation.

2. Materials and Research Methods

2.1. Configuration of the Ultrasonic Vibration-Assisted Milling System

The ultrasonic vibration-assisted milling (UVAM) system developed in this study was designed to transmit ultrasonic vibration directly to the workpiece during CNC milling of hardened 90CrSi cylindrical surfaces. The system consists of four main components: an ultrasonic generator, a piezoelectric transducer, a stepped ultrasonic horn, and the workpiece mounted on a specially designed fixture installed on a CNC milling machine.

The ultrasonic generator converts electrical energy from a conventional power supply into high-frequency electrical signals. These signals excite the piezoelectric transducer, which converts the electrical excitation into mechanical vibration through the inverse piezoelectric effect. The mechanical vibration generated by the transducer is transmitted to the horn and subsequently to the workpiece.

Unlike conventional ultrasonic milling systems where vibration is applied to the cutting tool, the present configuration applies vibration directly to the workpiece along the axial (Z) direction. This configuration is particularly suitable for machining cylindrical surfaces of hardened steel components such as punches and forming tools.

In addition to the difference in vibration transmission direction, the present workpiece-based configuration offers several practical advantages over conventional tool-side ultrasonic vibration systems. In tool-side approaches, ultrasonic excitation is typically introduced through rotating tool holders integrated with the spindle, which significantly increases system cost, structural complexity, and maintenance requirements. In contrast, the proposed configuration applies vibration to the workpiece through a stationary horn–fixture system mounted on the machine table, resulting in a more economical and easier-to-implement solution for industrial applications. Furthermore, eliminating rotating ultrasonic components improves system reliability by avoiding issues related to dynamic imbalance and electrical signal transmission in high-speed spindles. Importantly, this approach is particularly effective for mass production scenarios, where identical or standardized workpieces are machined in large quantities, such as tablet compression punches or sheet-metal forming tools. In such cases, once the horn–workpiece system is properly calibrated, the vibration conditions can be consistently reproduced across batches, thereby enhancing process stability, productivity, and overall manufacturing efficiency.

However, this configuration also involves certain trade-offs. The effectiveness of vibration transmission depends on the proper design and assembly of the horn-workpiece interface to minimize energy loss, and the approach may be less flexible than tool-side systems when machining complex free-form geometries. Nevertheless, for cylindrical and axisymmetric components, the proposed configuration provides a favorable balance between machining performance, system simplicity, cost-effectiveness, and scalability in industrial production.

The overall configuration of the ultrasonic vibration-assisted milling system is illustrated in Figure 2.

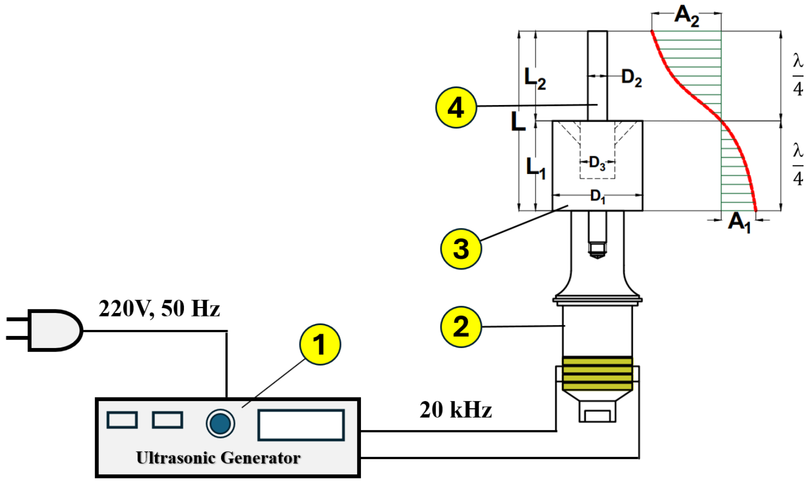

Figure 2. Configuration of the ultrasonic vibration-assisted milling system used in this study: (1) ultrasonic generator, (2) piezoelectric transducer, (3) ultrasonic horn acting as an amplitude amplifier, and (4) workpiece mounted in the horn.

2.2. Design Requirements and Assumptions

The ultrasonic horn and vibration transmission system were designed to satisfy several functional requirements. First, the system must operate at the resonance frequency of 20 kHz, which corresponds to the nominal frequency of the ultrasonic generator. Second, the horn must provide sufficient stiffness and mechanical strength to withstand machining loads during milling. Third, acoustic energy loss at the mounting interface must be minimized to ensure efficient vibration transmission.

In ultrasonic-assisted milling processes, vibration amplitudes typically range from 2 µm to 10 µm, which are sufficient to create intermittent cutting while maintaining machining stability. In this study, three vibration amplitudes were selected for experimental investigation: 4 µm, 6 µm, and 8 µm.

To simplify the initial acoustic design, the horn–workpiece system was modeled as a homogeneous and isotropic solid body. The theoretical analysis considered only longitudinal wave propagation, while the effects of transverse deformation, geometric discontinuities, and local contact conditions were neglected in the preliminary calculations.

2.3. Preliminary Theoretical Design of the Horn–Workpiece System

The preliminary design of the horn–workpiece system was based on the theory of longitudinal elastic wave propagation in solid materials. The wave velocity C in the material is expressed as [19]:

$$C = \sqrt{\frac{E}{\rho}}, \tag{1}$$

where E is the Young's modulus and ρ is the material density.

In this study, both the horn and the workpiece were manufactured from hardened 90CrSi tool steel. According to [20], most vibration-assisted machining processes use amplitudes of about 2–20 µm. Since the required amplitude in this study (4–8 µm) lies within this range, 90CrSi steel is sufficient, while also offering advantages in cost and material compatibility. The chemical composition of the 90CrSi steel is presented in Table 1. After quenching and tempering, the material achieved a hardness of 58–60 HRC, representing a typical condition for hardened tool steels used in industrial applications. The density of the material was experimentally determined as 7706 $\mathrm{kg/m^3}$, and the Young's modulus was taken as 205 GPa. Using these values, the ultrasonic wave velocity was calculated as

$$C = 5157.78 \ \mathrm{m/s}$$

Table 1. Chemical composition (wt. %) of 90CrSi tool steel used in this study [21].

Element	**C**	**Si**	**Cr**	**Mn**	**Ni**	**P**	**Mo**
Content (wt. %)	0.9263	1.341	1.030	0.4418	0.0298	0.0196	0.0081
Element	V	Cu	W	Ti	Al	Co	Fe
Content (wt. %)	0.0053	0.0675	0.0021	0.0063	0.0060	0.0073	95.4722

For the operating frequency $f = 20$ kHz, the corresponding wavelength is

$$\lambda = \frac{C}{f} \tag{2}$$

and we have

$$\lambda = 257.89 \ \mathrm{mm}.$$

To achieve resonance, the total length of the horn–workpiece system must correspond to half of the wavelength:

$$L = \frac{\lambda}{2} = 128.94 \ \mathrm{mm}. \tag{3}$$

Thus, the system can be divided into two quarter-wavelength segments:

$$L_1 = L_2 = \frac{\lambda}{4} = 64.47 \ \mathrm{mm}. \tag{4}$$

The flange used to mount the horn onto the fixture was placed at the vibration node, where the displacement amplitude is theoretically zero. Positioning the flange at the node reduces acoustic energy loss and prevents vibration transmission to the machine structure.

The theoretical model used for calculating the horn–workpiece resonance system is shown in Figure 3.

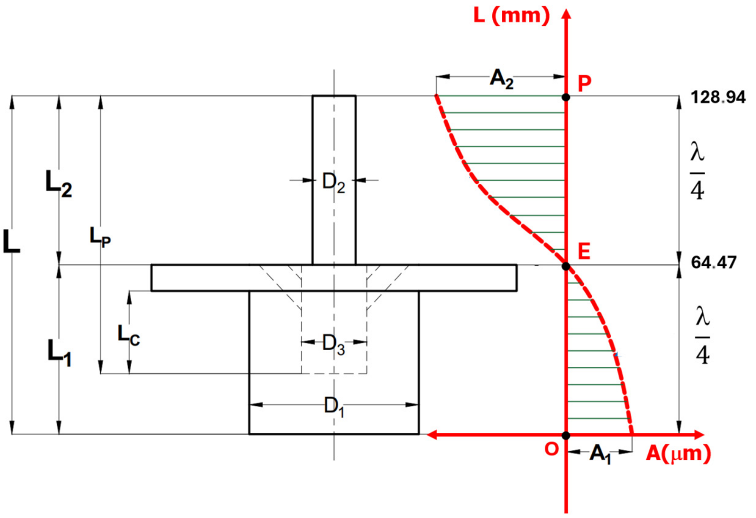

Figure 3. Theoretical model of the horn–workpiece system used for preliminary acoustic calculations.

2.4. Horn Geometry and Assembly Design

Based on the acoustic design and practical assembly requirements, a stepped cylindrical horn was selected. The horn geometry was designed to satisfy both vibration transmission efficiency and mechanical rigidity.

The outer diameter of the horn D_1 was selected as 65.0 mm, which ensures sufficient structural strength and allows the integration of a cavity used to clamp the workpiece shank. The machining head of the workpiece had a diameter of 16.5 mm, while the clamping shank had a diameter of 25.0 mm.

For the present ultrasonic system operating at approximately 20 kHz, the wavelength in the horn material (aluminum) is about $\lambda \approx 257.89$ mm, corresponding to a half-wavelength horn length of $L \approx 130$ mm. Therefore, the ratio $D_1/\lambda = 65/257.89 = 0.252$. According to [19], one-dimensional longitudinal wave propagation is valid when the transverse dimensions remain sufficiently small compared to the wavelength (typically $D < \lambda/4$). In this study, the selected horn diameter lies very close to this threshold, indicating that the system operates at the boundary of the slender rod approximation. Under such conditions, the longitudinal vibration mode remains dominant. However, transverse deformation induced by Poisson effects may still arise due to the intrinsic coupling between axial and lateral strain components. As reported in [22], Poisson's ratio governs the relationship between longitudinal and transverse deformation, and deviations from idealized assumptions may occur, particularly in regions with non-uniform stress distribution or localized strain gradients. Although the present horn operates mainly in the linear elastic regime, this implies that minor transverse motion cannot be entirely neglected. Nevertheless, since D_1 does not exceed the critical range ($\approx\lambda/3$) identified in [19], strong lateral coupling and spurious vibration modes are not expected to dominate the system response.

The machining head of the workpiece had a diameter of 16.5 mm, while the clamping shank had a diameter of 25.0 mm.

The horn was connected to the transducer through a 1/2″-20 UNF threaded joint, which ensures reliable mechanical coupling and prevents loosening during ultrasonic vibration. The horn also includes a mounting flange with a diameter of 140.0 mm, used to attach the horn assembly to the fixture.

2.5. Experimental Verification of the Resonant System

After fabrication, the ultrasonic vibration system was experimentally verified to confirm the resonance characteristics.

The axial vibration amplitude of the horn was measured using a non-contact fiber optic displacement sensor (Philtec D170-BEG1H, Annapolis, MD, USA). The sensor signal was acquired through a NI USB-6421 data acquisition (DAQ) system (National Instruments Corporation, Austin, TX, USA)with a sampling rate of 250 kS/s and processed using NI SignalExpress 2015 software.

The measurement uncertainty was estimated by considering the combined effects of sensor resolution, data acquisition accuracy, and signal noise. The fiber optic sensor provides sub-micrometer resolution, while the 16-bit DAQ system introduces negligible quantization error relative to the measured signal level. The high sampling rate (250 kS/s), which is more than ten times higher than the vibration frequency (~20 kHz), ensures accurate signal reconstruction according to the Nyquist criterion. Repeated measurements under steady-state conditions showed consistent amplitude values with minimal fluctuation.

Based on these factors, the overall measurement uncertainty is estimated to be within ±0.2 μm, corresponding to less than 5% of the experimental measured amplitude range (4–8 μm).

Next, the resonance characteristics of the horn-workpiece system were examined by frequency sweeping using a digital oscilloscope. The resonance peaks were detected near 20.001 kHz, confirming that the system operates very close to the target frequency.

The resonance verification procedure is illustrated in Figure 4.

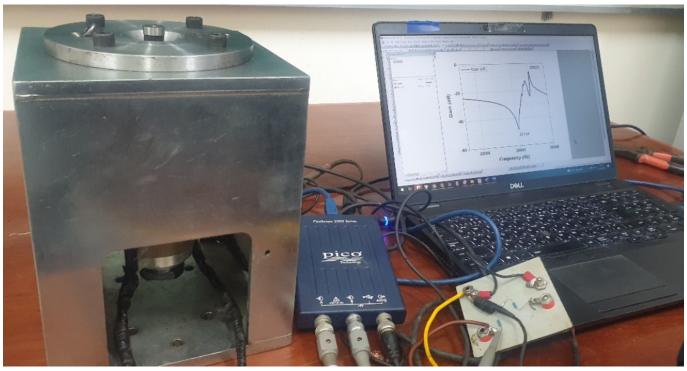

Figure 4. Experimental setup used to verify the resonance frequency of the horn–workpiece system.

The theoretical acoustic calculations were further validated by measuring the vibration period of the system. The measured vibration period was 50 µs, which agrees with the theoretical value corresponding to a frequency of 20 kHz.

The experimental measurement of the vibration signal is shown in Figure 5.

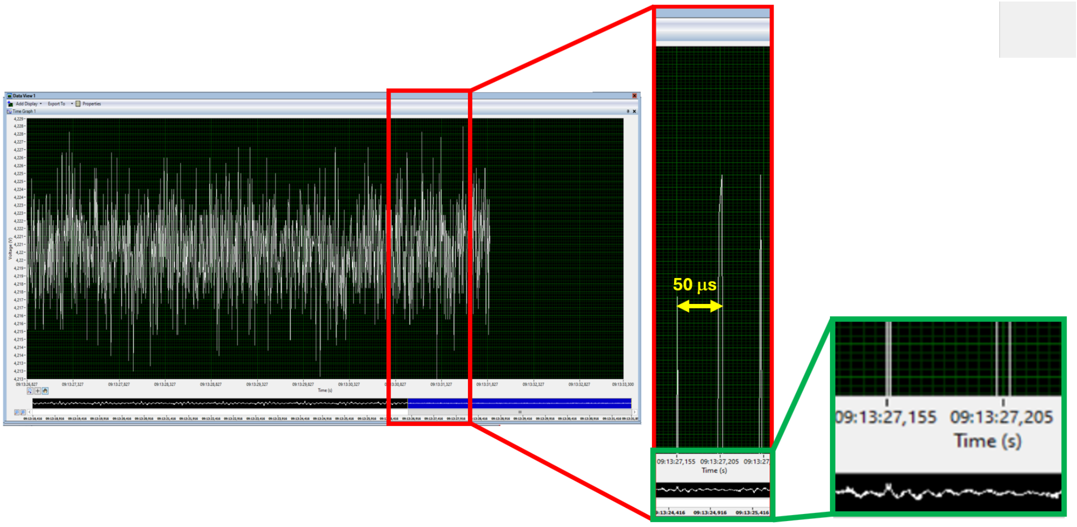

Figure 5. Oscilloscope measurement of the vibration period used to validate the acoustic calculations.

The resonance characteristics of the horn–workpiece system were further investigated through amplitude–frequency response analysis, as shown in Figure 6. The results illustrate the variation in vibration amplitude with excitation frequency for different workpiece lengths (Lp = 58, 62, and 66 mm).

It can be observed that each curve exhibits a clear and well-defined resonance peak in the vicinity of 19.4–19.6 kHz, indicating stable dynamic behavior of the system. Moreover, no significant secondary peaks are present, suggesting that spurious vibration modes are negligible. The operating frequency of approximately 20 kHz is located close to the resonance region, where the amplitude remains stable and controllable.

These findings confirm that the horn–workpiece system operates under a stable resonance condition, and that the selected working frequency ensures reliable vibration performance for subsequent machining experiments.

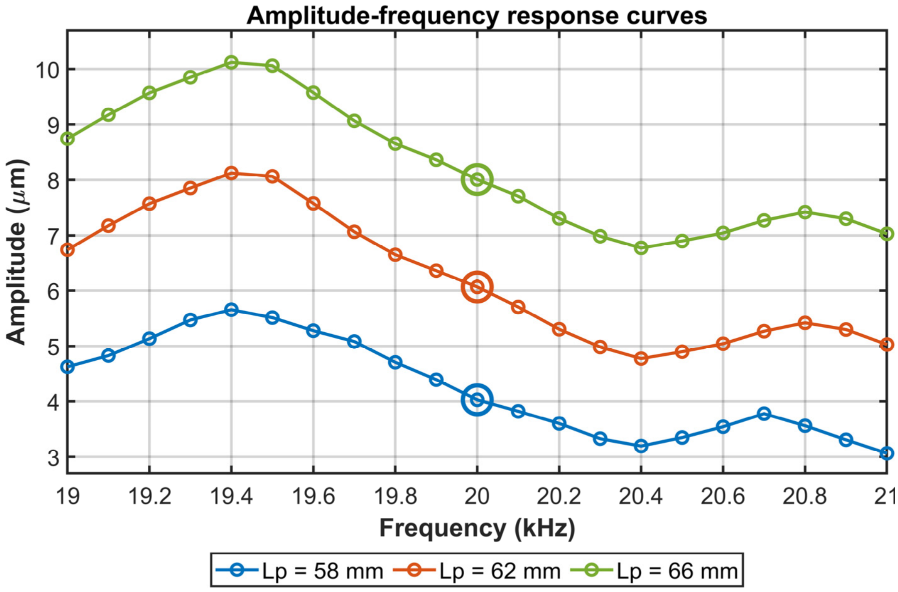

Figure 6. Amplitude–frequency response curves of the horn–workpiece system for different workpiece lengths (Lp). A clear resonance peak is observed near 20 kHz, indicating stable system behavior.

2.6. Two-Step Experimental Calibration of Workpiece Length

Although the horn length was fixed according to the resonance condition, the vibration amplitude at the machining surface can be adjusted by varying the workpiece length. Therefore, a two-step experimental procedure was used to determine the workpiece lengths corresponding to the target amplitudes.

Step 1: coarse screening

In the first step, 42 workpieces with lengths ranging from 54 mm to 136 mm were fabricated with a step size of 2 mm. The vibration amplitude at the workpiece tip was measured for each length using a fiber optic displacement sensor and a data acquisition system. To ensure measurement reliability, each experimental condition was repeated three times under steady-state vibration conditions. The reported amplitude values correspond to the average of these measurements. The variation between repeated measurements was small, indicating good repeatability and stability of the measurement system.

The relationship between workpiece length and vibration amplitude at a frequency of 20 kHz is shown in Figure 7.

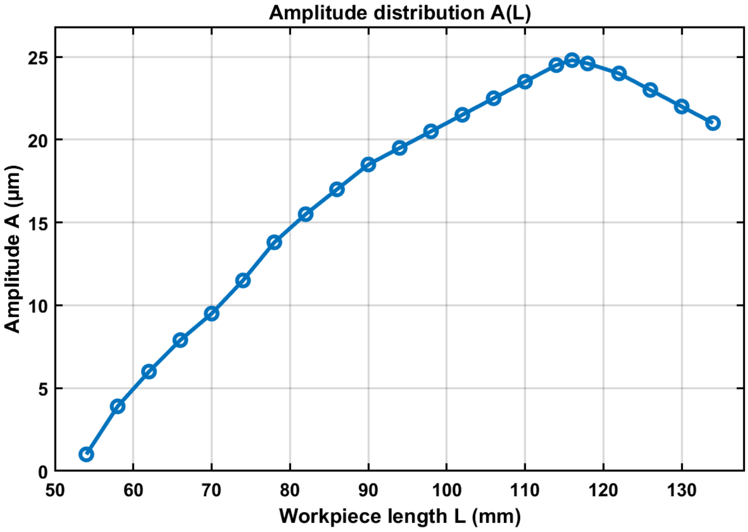

Figure 7. Relationship between workpiece length and ultrasonic vibration amplitude.

The results showed that the maximum amplitude of approximately 24.8 µm occurred at a workpiece length near 116 mm, while the amplitude range suitable for milling (4–8 µm) occurred within the shorter length interval of 56–70 mm.

Step 2: fine calibration

In the second step, workpieces were fabricated with a finer increment of 1 mm within the identified length range. This calibration allowed precise determination of the workpiece lengths corresponding to the target amplitudes.

The experimental calibration showed that the target vibration amplitudes could be achieved by varying the workpiece length, with amplitudes of 4 µm, 6 µm, and 8 µm corresponding to workpiece lengths of 58 mm, 62 mm, and 66 mm, respectively.

The horn–workpiece configurations used to generate these amplitudes are illustrated in Figure 8.

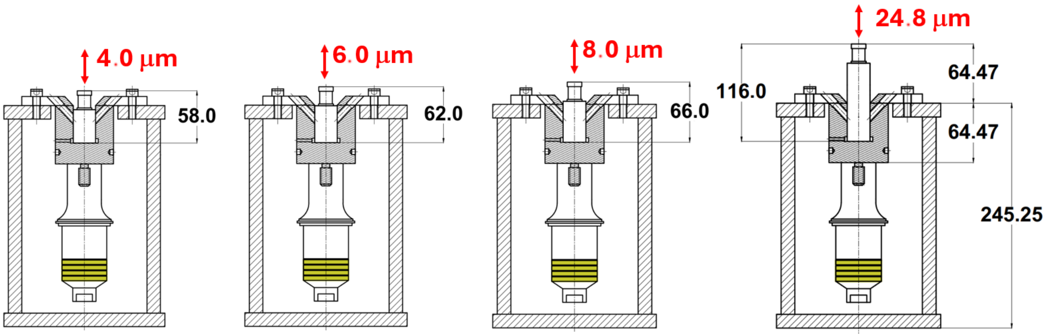

Figure 8. Horn–workpiece configurations producing different ultrasonic vibration amplitudes.

2.7. Final Specification of the Ultrasonic Vibration System

Based on the theoretical design and experimental calibration, the ultrasonic vibration system used in the milling experiments operates at a frequency of 20 kHz with a horn length of 64.47 mm and a total resonant system length of 128.94 mm. The maximum vibration amplitude measured at the workpiece end was approximately 24.8 µm. Three amplitudes, 4 µm, 6 µm, and 8 µm, were selected for the milling experiments, corresponding to workpiece lengths of 58 mm, 62 mm, and 66 mm, respectively. During operation, the ultrasonic generator was set to a power level of 60% to ensure stable vibration.

This design approach, combining theoretical acoustic modeling with experimental calibration, ensures that the ultrasonic vibration system operates at resonance and provides stable vibration amplitudes suitable for ultrasonic vibration-assisted milling of hardened 90CrSi cylindrical surfaces.

3. Experimental Setup and Milling Conditions

3.1. Experimental Setup

The experimental investigation was conducted to evaluate and optimize the machining performance during ultrasonic vibration-assisted milling (UVAM) of hardened 90CrSi tool steel cylindrical surfaces. The experimental setup used in this study is illustrated in Figure 9.

The experiments were carried out on a vertical CNC milling machine equipped with a high-frequency ultrasonic vibration system. The ultrasonic system consisted of an ultrasonic generator (MPI WG-3000, Le Lode, Switzerland, rated power 3000 W), a piezoelectric transducer (RPS-5020-4Z, operating frequency 20 kHz, power 1500 W, RPS-SONIC/Hangzhou Powersonic Equipment Co., Ltd., Hangzhou, China), and a stepped horn made of 90CrSi tool steel. The horn was designed to amplify and transmit longitudinal ultrasonic vibration directly to the workpiece mounted in the horn cavity.

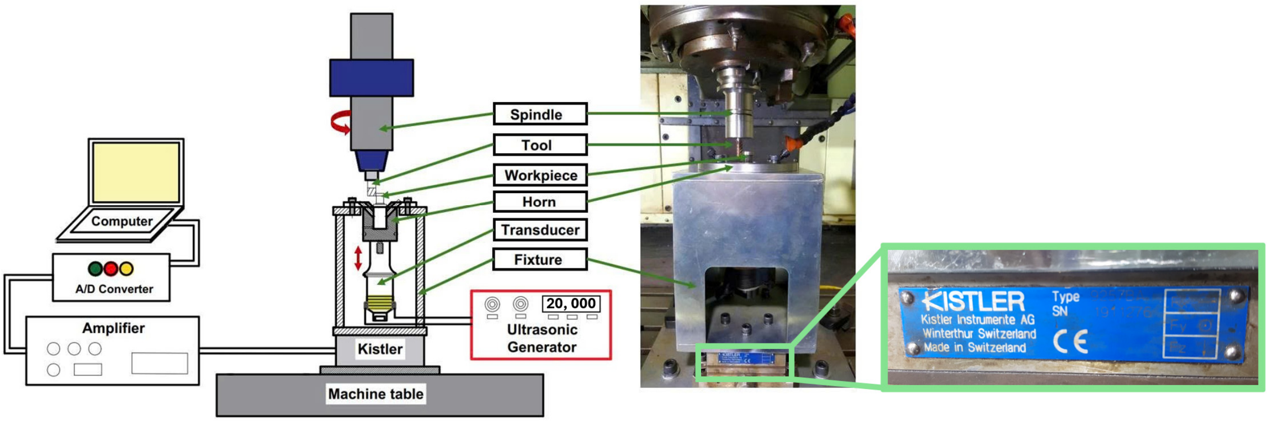

Figure 9. Experimental setup of the ultrasonic vibration-assisted milling system.

During machining, the cylindrical workpiece was clamped inside the horn and vibrated along the axial direction. A solid carbide end mill was used to machine the cylindrical surface of the specimen. To ensure stable cutting conditions and facilitate chip removal, a conventional flood coolant system was applied throughout the milling process.

3.2. Workpiece Material and Geometry

The workpiece material used in the experiments was hardened 90CrSi tool steel, which is widely applied in industrial components such as punches, dies, and forming tools due to its high hardness and wear resistance.

In this study, cylindrical workpieces were prepared to simulate practical industrial components with profiled cylindrical surfaces. The geometry and dimensions of the test specimens are presented in Figure 10.

(**a**) (**b**)

Figure 10. Geometry and physical appearance of the cylindrical 90CrSi steel workpieces: (**a**) dimensional drawing; (**b**) actual photograph of the prepared specimens.

Each specimen consisted of a cylindrical section used as the machining surface and a shank portion used for mounting in the horn. The cylindrical surface of the specimen served as the main machining region during the ultrasonic vibration-assisted milling experiments.

3.3. Design of Experiments

The experimental design was developed using the Box–Behnken design (BBD) methodology. This design approach allows efficient construction of second-order response surface models with a reduced number of experimental trials.

In the experimental design, four process parameters were considered as independent variables: ultrasonic vibration amplitude A (µm), cutting speed V_c (m/min), feed rate V_f (mm/min), and radial depth of cut a_e (mm).

Each factor was investigated at three coded levels, and a total of 29 experimental runs were conducted. The experimental design included five replicates at the center point to evaluate experimental error and assess model curvature.

The Box–Behnken design enables systematic investigation of the interaction effects among machining parameters and provides reliable data for constructing predictive models used in the subsequent optimization process.

3.4. Evaluation of Machining Performance

Two performance indicators were used to evaluate the milling process: material removal rate (MRR) and surface roughness (Ra).

Material removal rate:

Material removal rate was used as the primary productivity indicator. It was calculated using a mass-based approach according to the following equation:

$$MRR = \frac{\mathrm{m_{before}} - \mathrm{m_{after}}}{\mathrm{t}}, \tag{5}$$

where m_{before} and m_{after} are the masses of the workpiece before and after machining, respectively, measured using a precision balance (WT3003NE) with an accuracy of ±0.001 g. The variable t represents the machining time in minutes, which was determined based on the machining program executed on the CNC milling machine.

This mass-based method provides accurate quantification of the removed material volume under varying cutting conditions.

Surface roughness:

Surface roughness *Ra* was used to evaluate the quality of the machined cylindrical surfaces. Measurements were performed using a Mitutoyo SJ-410 surface roughness tester (Mitutoyo Corporation, Kawasaki, Japan). For each experimental run, three measurements were taken at different locations along the circumference of the machined surface, and the average value was used for further analysis.

3.5. Experimental Design Matrix

The complete experimental matrix, including the process parameters and the measured responses, is presented in Table 2. The table lists the combinations of ultrasonic vibration amplitude, cutting speed, feed rate, and radial depth of cut used in the experiments, together with the corresponding measured values of MRR and surface roughness *Ra*.

Table 2. This experimental design matrix (BBD) and measured responses (MRR and Ra) for ultrasonic vibration-assisted milling of hardened 90CrSi cylindrical surfaces.

No.	A (µm)	V_c (m/min)	V_f (mm/min)	a_e (mm)	MRR (g/min)	R_a (µm)
1	4	125	1327	0.10	3.104	0.384
2	8	125	1327	0.10	3.099	0.395
3	8	125	1592	0.15	5.390	0.436
4	6	125	1592	0.10	4.644	0.406
5	4	100	1327	0.15	4.633	0.410
6	6	125	1062	0.20	5.226	0.453
7	4	125	1062	0.15	3.692	0.437
8	6	150	1327	0.20	6.466	0.466
9	6	150	1062	0.15	4.036	0.423
10	6	125	1062	0.10	2.830	0.371
11	6	100	1327	0.10	3.269	0.398
12	6	100	1592	0.15	5.788	0.451

Table 2. *Cont.*

No.	A (µm)	V_c (m/min)	V_f (mm/min)	a_e (mm)	MRR (g/min)	R_a (µm)
13	6	100	1062	0.15	3.747	0.435
14	8	125	1327	0.20	6.452	0.475
15	4	150	1327	0.15	4.835	0.365
16	6	125	1327	0.15	4.599	0.389
17	6	125	1327	0.15	4.707	0.393
18	6	125	1327	0.15	4.404	0.380
19	4	125	1327	0.20	6.602	0.473
20	8	150	1327	0.15	4.467	0.372
21	4	125	1592	0.15	5.640	0.444
22	8	100	1327	0.15	4.359	0.402
23	6	125	1592	0.20	7.394	0.485
24	6	100	1327	0.20	6.335	0.474
25	6	150	1592	0.15	5.802	0.440
26	8	125	1062	0.15	3.632	0.444
27	6	150	1327	0.10	3.335	0.381
28	6	125	1327	0.15	4.816	0.386
29	6	125	1327	0.15	4.743	0.387

These experimental data were subsequently used to develop response surface models and to perform multi-objective optimization of the milling process.

4. Multi-Objective Optimization of Milling Parameters

4.1. Surrogate-Based Formulation of the Optimization Problem

The multi-objective optimization problem was formulated using the experimental dataset obtained from the Box–Behnken design in Section 3. Four machining parameters were treated as decision variables, namely ultrasonic vibration amplitude A, cutting speed V_c, feed rate V_f, and radial depth of cut a_e. Their lower and upper bounds were directly defined from the experimental design space, i.e., $A = 4\text{–}8$ µm, $V_c = 100\text{–}150$ m/min, $V_f = 1062\text{–}1592$ mm/min, and $a_e = 0.10\text{–}0.20$ mm.

Two response variables were considered in the optimization process: the material removal rate (MRR), which should be maximized to improve productivity, and the surface roughness Ra, which should be minimized to improve surface quality. Accordingly, the optimization problem can be expressed as

$$\max \mid MRR\left(A, V_c, V_f, a_e\right), \tag{6}$$

$$\min \mid Ra\left(A, V_c, V_f, a_e\right), \tag{7}$$

subject to the variable bounds defined above.

Because NSGA-II requires repeated evaluation of the objective functions, surrogate models were first developed to approximate the two responses. In the Matlab version 24.2.0.2923080 implementation, both second-order response surface methodology (RSM) models and Gaussian process regression (GPR) models were constructed. The quadratic RSM models were fitted using fitlm (…, ‘quadratic’), whereas the GPR models were built using an automatic relevance determination squared-exponential kernel (ardsquaredexponential) with standardized inputs and a constant basis function. Model performance was evaluated using the coefficient of determination $\left(R^2\right)$, root-mean-square error (RMSE), and mean absolute error (MAE), both on the training set and under five-fold cross-validation.

To assess the predictive performance of the developed surrogate models, both RSM and GPR were evaluated using the coefficient of determination (R^2) and root mean square error (RMSE), together with k-fold cross-validation. For the RSM models, the training results yielded R^2 values of 0.9572 and 0.9486, with RMSE values of 0.2684 and 0.00691 for MRR and Ra, respectively. In comparison, the GPR models exhibited higher predictive accuracy, with R^2 values of 0.9895 and 0.9889, and RMSE values of 0.1202 and 0.00377 for MRR and Ra, respectively. Cross-validation results further confirmed this trend. The RSM models showed R^2 values of 0.9023 for MRR and 0.6527 for Ra, with RMSE values of 0.3876 and 0.0219, respectively. In contrast, the GPR models achieved higher generalization performance, with R^2 values of 0.9545 for MRR and 0.7615 for Ra, and corresponding RMSE values of 0.2505 and 0.0175.

These results indicate that the GPR models provide superior predictive capability, particularly in capturing nonlinear relationships and maintaining robustness with a limited dataset. Therefore, the final NSGA-II search was performed using GPR-predicted values of MRR and Ra as the objective functions.

For the optimization algorithm, the objective vector was defined in minimization form as

$$\mathrm{f}(\mathrm{x}) = \left[-\widehat{MRR}(\mathrm{x}), \widehat{Ra}(\mathrm{x})\right], \tag{8}$$

where $\mathbf{x} = \left[A, V_c, V_f, a_e\right]$, $\widehat{MRR}$ is the GPR-predicted material removal rate, and $\widehat{Ra}$ is the GPR-predicted surface roughness. By minimizing $-\widehat{MRR}$, the algorithm effectively maximizes MRR while simultaneously minimizing Ra.

4.2. NSGA-II Implementation

The multi-objective search was carried out using the Matlab function gamultiobj, which implements the NSGA-II algorithm. The optimization was performed with four decision variables, a population size of 120, and a maximum of 120 generations. The main algorithmic settings were a Pareto fraction of 0.7, a crossover fraction of 0.8, and a function tolerance of 10^{-6}. These settings provide a sufficiently large search space exploration while maintaining stable convergence of the non-dominated set.

At each generation, the objective values of the population were evaluated using the GPR surrogate models. The current non-dominated solutions were then identified and stored through a custom output function. In addition to the Pareto solutions themselves, the code also recorded several generation-wise performance metrics, including hypervolume, convergence metric, spacing, spread, and inverted generational distance (IGD). This allowed the evolution of the Pareto front to be monitored throughout the optimization process rather than only examining the final generation.

The use of NSGA-II is appropriate in the present study because the two objectives are inherently conflicting. In general, increasing MRR tends to require more aggressive cutting conditions, which may deteriorate the surface finish and increase Ra. Therefore, instead of a single absolute optimum, the algorithm yields a set of non-dominated solutions representing different trade-offs between productivity and surface quality.

4.3. Evolution and Convergence Behavior of NSGA-II

The generation-wise behavior of the NSGA-II optimization can be evaluated from both the hypervolume history (Figure 11) and the snapshots of the Pareto front (Figure 12). The hypervolume metric, which measures the dominated objective space relative to a reference point, provides a quantitative indicator of both convergence and diversity of the non-dominated solutions.

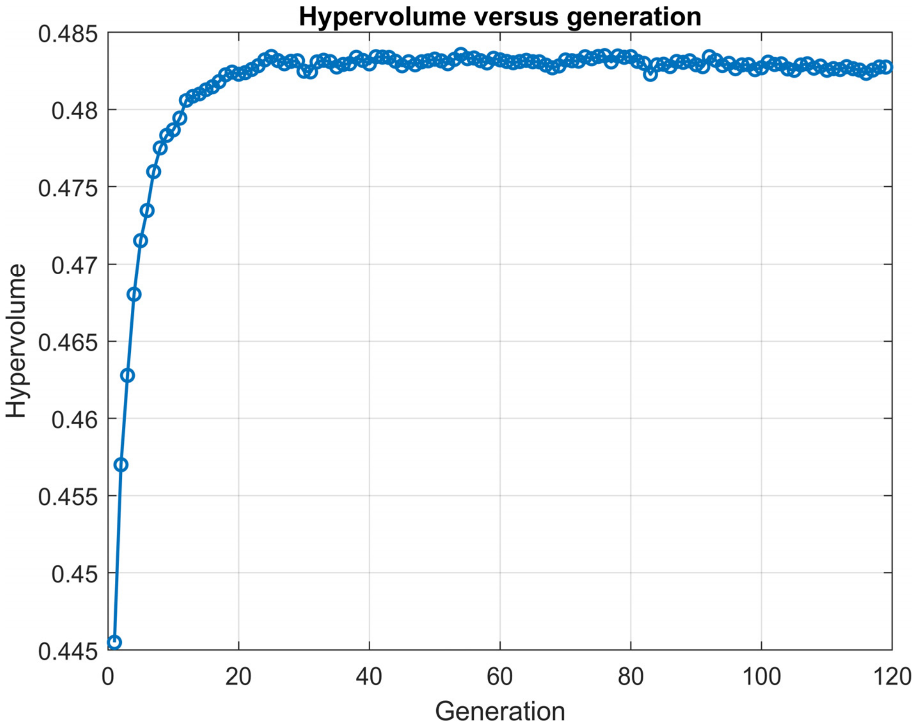

Figure 11. Hypervolume versus generation for the GPR-assisted NSGA-II optimization.

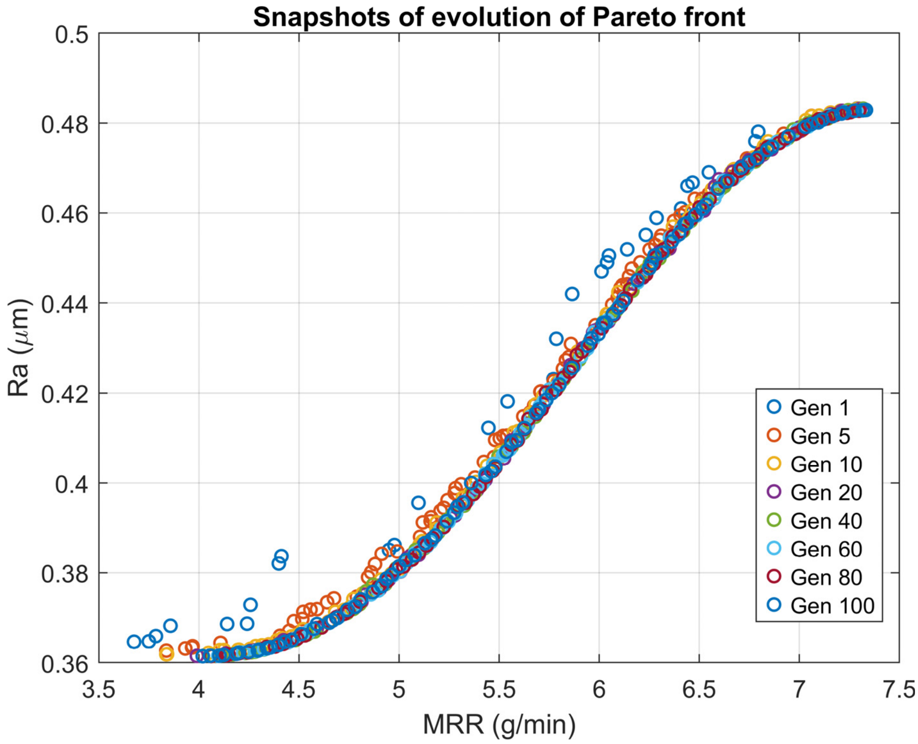

Figure 12. Snapshots of the evolution of the Pareto front at selected generations during the GPR-assisted NSGA-II process.

The hypervolume history is presented in Figure 11. It can be observed that the hypervolume increased rapidly during the early generations, rising from approximately 57.4 at the first generation to around 62.0 within the first 20 generations. This indicates that the algorithm quickly identified substantially improved non-dominated solutions in the initial search stage. After this rapid improvement, the hypervolume continued to grow more gradually and approached a nearly stable value of about 63.0 toward the final generations. The stabilization observed after approximately 60–80 generations suggests that the optimization process had largely converged and that further generations mainly produced small refinements of the Pareto front rather than major improvements.

A complementary view of the search behavior is provided by the evolution snapshots of the Pareto front shown in Figure 12. In the early generations, the solution set was more scattered and farther from the final frontier. As the number of generations increased, the front gradually moved toward a more consistent and smoother trade-off curve. By around generation 60, the front was already close to its final form, and only minor refinements were observed between generations 80 and 120. This behavior is consistent with the hypervolume trend and confirms that the selected NSGA-II settings were adequate to reach a stable non-dominated solution set.

The consistency between the hypervolume trend and the Pareto front evolution confirms that the optimization process is both stable and reliable. These figures collectively demonstrate that the GPR-assisted NSGA-II framework is capable of efficiently exploring the design space and converging toward a well-defined set of optimal trade-off solutions.

Although only the hypervolume and the front snapshots are presented here, the Matlab code also tracked additional convergence-related metrics such as convergence distance, spacing, spread, and IGD. These metrics further support the overall stability of the optimization process and can be reported in a supplementary table if a more detailed convergence analysis is desired.

4.4. Final Pareto Front and Trade-Off Analysis

The final Pareto front obtained from the GPR-assisted NSGA-II optimization is shown in Figure 13. The Pareto solutions clearly illustrate the trade-off between material removal rate and surface roughness. The MRR values range approximately from 4.0 g/min to about 7.3 g/min, while the corresponding surface roughness values vary between 0.36 μm and 0.48 μm.

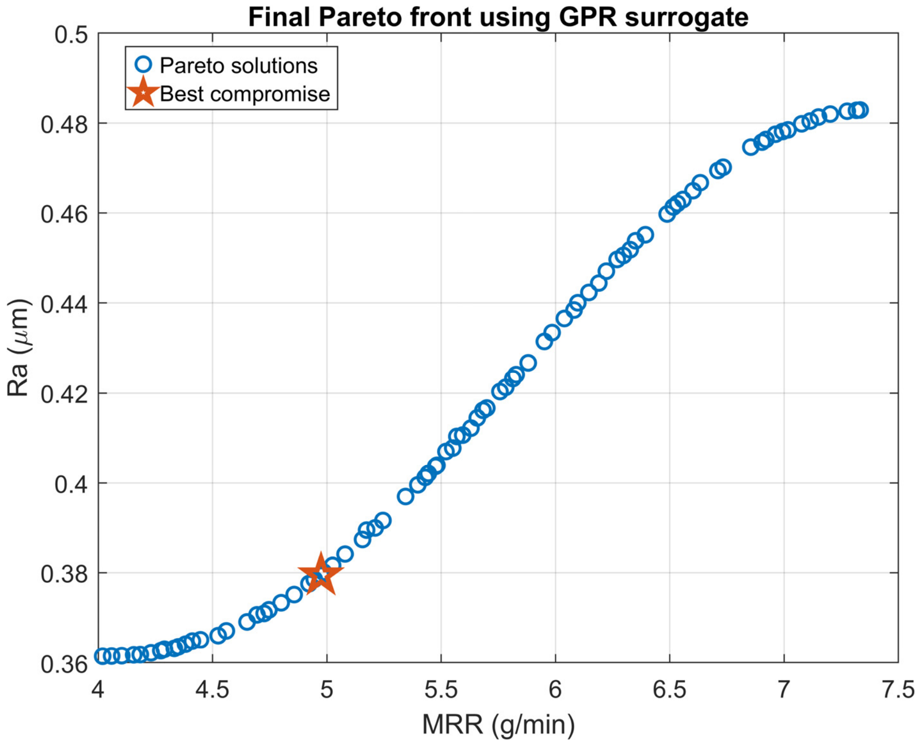

Figure 13. Final Pareto front obtained by the GPR-assisted NSGA-II optimization for simultaneous maximization of MRR and minimization of *Ra*.

At the left side of the Pareto front, lower surface roughness values are achieved but with relatively small MRR values. Conversely, the right side of the frontier corresponds to higher productivity but also higher surface roughness. This trade-off behavior indicates that maximizing productivity inevitably leads to a deterioration of surface quality.

Using equal weighting for the two objectives, a representative best-compromise solution was identified from the final Pareto set according to the score defined as $Score = 0.5\,MRR_{norm} + 0.5\,Ra_{norm}$. The corresponding machining parameters were $A = 4.72$ µm, $V_c = 148.674$ m/min, $V_f = 1379.165$ mm/min, and $a_e = 0.152$ mm. Under these conditions, the predicted responses are $MRR = 4.975$ g/min and $Ra = 0.3795$ µm. This solution is indicated by the star marker in Figure 12 and represents the best compromise between productivity and surface quality when the two objectives are considered equally important.

From a machining perspective, this compromise point lies in the central region of the Pareto frontier, where a noticeable increase in material removal rate can still be achieved without causing a significant deterioration in surface roughness, making it particularly suitable for balanced machining performance.

Therefore, selecting a suitable compromise solution from the Pareto set is essential for practical machining applications.

4.5. AHP-Based Weighting of Optimization Objectives

Although the Pareto front provides a set of non-dominated solutions, a decision-making method is required to select a preferred solution for practical machining applications. In this study, the Analytic Hierarchy Process (AHP) was employed to determine the relative importance of the two optimization objectives: maximizing the material removal rate (MRR) and minimizing the surface roughness Ra.

The pairwise comparison between the two objectives was expressed using the following comparison matrix

$$\mathbf{P} = \begin{bmatrix} 1 & 3 \\ \frac{1}{3} & 1 \end{bmatrix}, \tag{9}$$

where the element p_{ij} represents the relative importance of objective i over objective j. The value $p_{12} = 3$ indicates that the material removal rate is considered three times more important than surface roughness in the decision-making process.

Using the eigenvector method of AHP, the priority weights of the objectives were obtained as

$$w_{MRR} = 0.75, w_{Ra} = 0.25, \tag{10}$$

These weights indicate that productivity is given higher importance than surface quality in the optimization framework, which is consistent with practical machining considerations where production efficiency often plays a dominant role.

To evaluate the overall performance of each Pareto solution, the objective values were first normalized. The normalized values were calculated as

$$MRR_{norm} = \frac{MRR - MRR_{min}}{MRR_{max} - MRR_{min}}, \tag{11}$$

$$Ra_{norm} = \frac{Ra_{max} - Ra}{Ra_{max} - Ra_{min}}, \tag{12}$$

The overall AHP score of each Pareto solution was then computed using the weighted aggregation

$$Score = 0.75\,MRR_{norm} + 0.25\,Ra_{norm}, \tag{13}$$

where higher scores indicate better compromise solutions.

4.6. Ranking of Pareto Solutions and Preferred Machining Parameters

Based on the AHP score defined above, the Pareto solutions were ranked in descending order. The ranking results of the best solutions are illustrated in Figure 14, where the AHP scores gradually decrease with increasing rank.

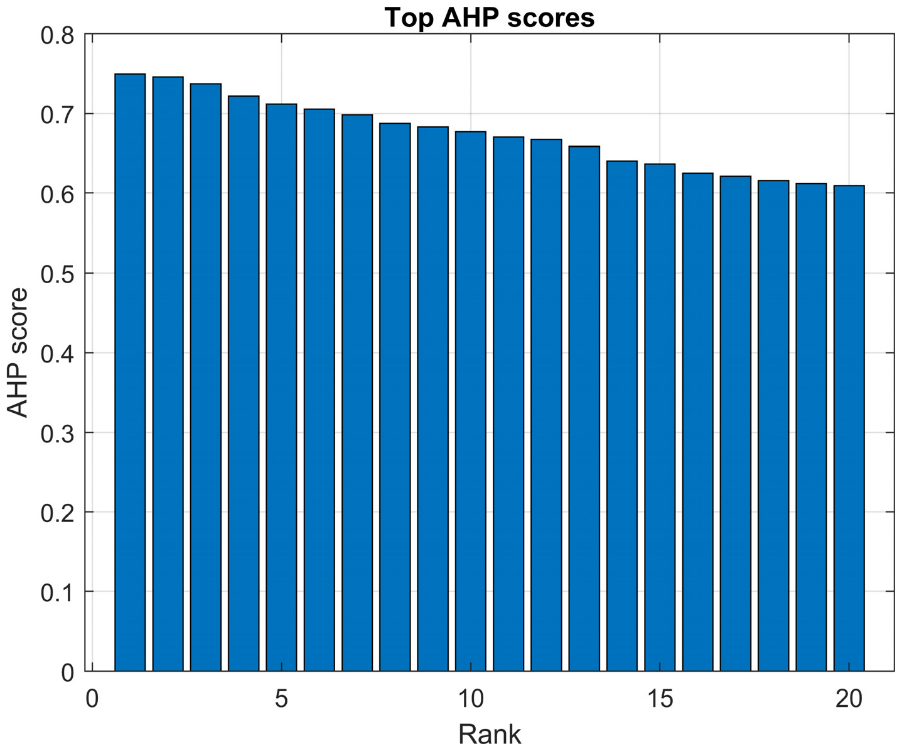

Figure 14. Ranking of the top Pareto solutions according to the AHP score.

The highest AHP score obtained among the Pareto solutions was approximately 0.75, corresponding to the most favorable balance between machining productivity and surface quality.

The preferred solution selected from the Pareto set is highlighted in Figure 15, where the star marker indicates the AHP-selected optimal solution on the Pareto front.

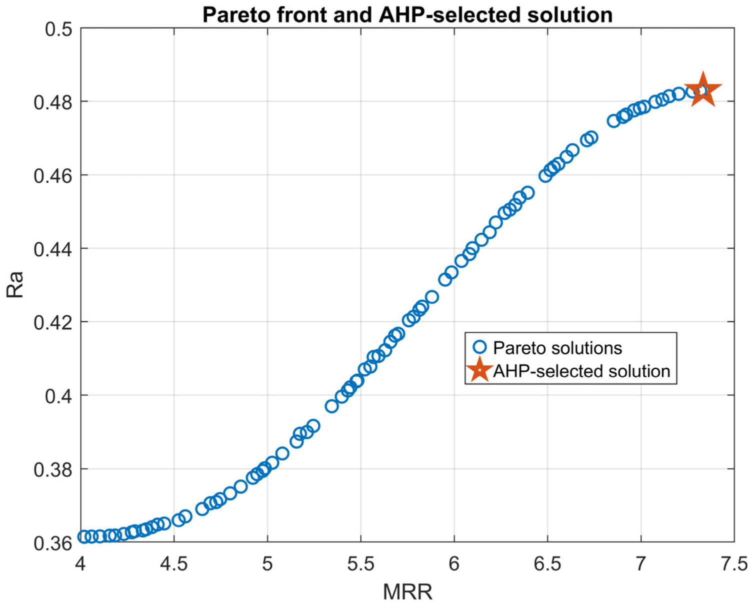

Figure 15. Pareto front and AHP-selected preferred solution.

The optimal machining parameters obtained from the AHP-selected Pareto solution correspond to an ultrasonic vibration amplitude of $A = 5.022$ μm, a cutting speed of $V_c = 148.055$ m/min, a feed rate of $V_f = 1561.826$ mm/min, and a radial depth of cut of $a_e = 0.1999$ mm. Under these conditions, the predicted machining performance indicates a material removal rate of $MRR = 7.332$ g/min with a surface roughness of $Ra = 0.4829$ μm.

The selected point lies near the knee region of the Pareto front, where a relatively large improvement in MRR can be achieved with only a moderate increase in surface roughness. This solution lies near the high-productivity region of the Pareto front, providing a substantial increase in material removal rate while maintaining acceptable surface quality. Therefore, this solution represents an effective compromise between machining efficiency and surface finish for ultrasonic vibration-assisted CNC milling of hardened 90CrSi cylindrical surfaces.

To validate the reliability of the surrogate-based optimization, confirmatory experiments were conducted using the optimal machining parameters obtained from the NSGA-II results. The selected conditions were ultrasonic vibration amplitude A = 5.0 μm, cutting speed $V_c = 148.1$ m/min, feed rate $V_f = 1561.83$ mm/min, and radial depth of cut $a_e = 0.2$ mm.

Each experiment was repeated three times under steady-state conditions, and the reported values correspond to the average results. The experimental outcomes yielded a material removal rate of MRR = 7.254 g/min and a surface roughness of Ra = 0.463 μm.

A comparison with the predicted optimal values shows small deviations, with relative errors of 1.064% for MRR and 4.298% for Ra. This good agreement confirms the accuracy of the developed surrogate models and the effectiveness of the proposed optimization framework.

Discussion of the optimal trade-off solution

The selected optimal solution lies in the high-productivity region of the Pareto frontier, where the material removal rate approaches its maximum attainable value within the studied design space while maintaining an acceptable level of surface roughness. This behavior reflects the inherent trade-off between productivity and surface quality in ultrasonic vibration-assisted milling. Increasing the feed rate and cutting speed tends to improve the material removal rate, but may also increase the resulting surface roughness due to higher cutting energy and tool–workpiece interaction. The AHP-selected solution therefore represents a balanced compromise that prioritizes productivity while still maintaining satisfactory surface integrity. From a practical machining perspective, this parameter combination provides a suitable operating condition for achieving efficient and stable milling of hardened 90CrSi cylindrical surfaces under ultrasonic vibration assistance.

4.7. Comparative Analysis of Ultrasonic-Assisted and Conventional Milling

To further evaluate the effect of ultrasonic vibration, a comparative analysis between ultrasonic-assisted milling and conventional milling (A = 0) was conducted. A separate set of experiments was performed using the same Box–Behnken design and identical machining parameters, with the only difference being the absence of ultrasonic vibration.

The comparison results are summarized in Table 3, which presents the percentage variation in material removal rate (MRR), surface roughness (Ra), and cutting force (F) for all experimental runs. It can be clearly observed that ultrasonic assistance leads to consistent improvements in machining performance across the entire design space.

Table 3. Comparison between conventional milling (A = 0) and ultrasonic-assisted milling, showing the percentage increase in MRR and reduction in Ra for all experimental runs.

No.	V (m/p)	Vf (mm/p)	ae (mm)	Without UV			With UV			Effectiveness		
				MRR (g/min)	Ra (µm)	F (N)	MRR (g/min)	Ra (µm)	F (N)	MRR Increase (%)	Ra Reduction (%)	F Reduction (%)
1	125	1327	0.10	2.146	0.560	112.419	3.104	0.384	74.514	30.86	31.48	33.72
2	125	1327	0.10	2.389	0.586	73.693	3.099	0.395	58.461	22.91	32.60	20.67
3	125	1592	0.15	4.052	0.680	122.117	5.390	0.436	93.606	24.82	35.90	23.35
4	125	1592	0.10	4.107	0.685	112.572	4.644	0.406	96.474	11.56	40.75	14.30
5	100	1327	0.15	3.091	0.590	142.516	4.633	0.410	92.402	33.28	30.46	35.16
6	125	1062	0.20	3.951	0.707	156.620	5.226	0.453	120.706	24.39	35.88	22.93
7	125	1062	0.15	2.756	0.671	136.551	3.692	0.437	99.846	25.36	34.87	26.88
8	150	1327	0.20	4.931	0.718	156.485	6.466	0.466	118.407	23.74	35.13	24.33
9	150	1062	0.15	3.436	0.678	114.514	4.036	0.423	95.484	14.87	37.62	16.62
10	125	1062	0.10	2.111	0.569	108.546	2.830	0.371	79.276	25.41	34.82	26.97
11	100	1327	0.10	2.638	0.627	112.055	3.269	0.398	90.149	19.30	36.56	19.55
12	100	1592	0.15	4.392	0.710	149.612	5.788	0.451	118.490	24.11	36.52	20.80
13	100	1062	0.15	2.902	0.685	99.789	3.747	0.435	79.505	22.55	36.49	20.33
14	125	1327	0.20	5.578	0.767	156.193	6.452	0.475	131.414	13.54	38.04	15.86
15	150	1327	0.15	3.316	0.529	154.812	4.835	0.365	101.134	31.42	30.96	34.67
16	125	1327	0.15	3.247	0.585	163.333	4.599	0.389	109.640	29.39	33.47	32.87
17	125	1327	0.15	3.412	0.598	155.922	4.707	0.393	108.674	27.50	34.29	30.30
18	125	1327	0.15	3.176	0.574	157.066	4.404	0.380	109.192	27.88	33.81	30.48
19	125	1327	0.20	4.228	0.679	211.380	6.602	0.473	134.015	35.96	30.39	36.60
20	150	1327	0.15	3.795	0.596	102.778	4.467	0.372	87.397	15.05	37.63	14.97
21	125	1592	0.15	3.866	0.641	151.379	5.640	0.444	98.841	31.45	30.68	34.71
22	100	1327	0.15	2.723	0.572	144.783	4.359	0.402	91.132	37.54	29.76	37.06
23	125	1592	0.20	6.594	0.873	160.211	7.394	0.485	137.463	10.81	44.44	14.20
24	100	1327	0.20	4.811	0.756	159.282	6.335	0.474	129.019	24.06	37.29	19.00
25	150	1592	0.15	4.670	0.701	119.677	5.802	0.440	96.598	19.51	37.20	19.28
26	125	1062	0.15	2.173	0.609	166.597	3.632	0.444	95.547	40.17	27.11	42.65
27	150	1327	0.10	2.525	0.597	100.233	3.335	0.381	78.510	24.30	36.16	21.67
28	125	1327	0.15	3.622	0.602	73.366	4.816	0.386	56.329	24.78	35.89	23.22
29	125	1327	0.15	3.337	0.574	84.478	4.743	0.387	56.351	29.63	32.58	33.30

Specifically, the material removal rate (MRR) increased in the range of 10.81% to 40.17%, while the surface roughness (Ra) decreased by 27.11% to 44.44% compared to conventional milling. In addition, the cutting force (F) was significantly reduced, with a decrease ranging from 14.2% to 42.65% under ultrasonic-assisted conditions.

These improvements were consistently observed for all experimental runs, indicating that the enhancements in machining performance are primarily attributed to the presence of ultrasonic vibration rather than variations in process parameters. The reduction in cutting force can be associated with the intermittent cutting mechanism induced by ultrasonic vibration, which facilitates chip separation and reduces tool–workpiece interaction forces. Consequently, the combined effects of increased MRR, reduced Ra, and lower cutting force confirm the effectiveness of ultrasonic vibration in improving both machining efficiency and surface integrity.

Overall, the results presented in Table 2 provide strong experimental evidence supporting the beneficial role of ultrasonic vibration in machining hardened 90CrSi steel under the investigated conditions.

5. Conclusions

In summary, this study has demonstrated a comprehensive framework for ultrasonic vibration-assisted CNC milling of hardened 90CrSi cylindrical surfaces, integrating system design, experimental validation, and multi-objective optimization. The proposed workpiece-based ultrasonic vibration configuration, combined with a quarter-wavelength horn–workpiece system and two-step amplitude calibration, enables stable and controllable vibration conditions suitable for cylindrical surface machining.

The surrogate modeling and optimization results confirm that the GPR-assisted NSGA-II approach provides reliable and accurate prediction of machining performance, as validated by experimental tests with deviations below 5%. In addition, the comparative analysis between ultrasonic-assisted and conventional milling clearly demonstrates the effectiveness of ultrasonic vibration, with MRR increasing by 10.81–40.17%, Ra decreasing by 27.11–44.44%, and cutting force reduced by 14.2–42.65% across all experimental runs.

These findings provide both quantitative evidence and practical insights into the role of ultrasonic vibration in improving machining efficiency and surface quality for hardened cylindrical components. However, it should be noted that the present study focuses on MRR, Ra, and cutting force as performance indicators, while other aspects such as tool wear and thermal effects were not investigated.

Future work will focus on extending the experimental framework to include additional process indicators and more complex geometries, as well as further investigating the dynamic behavior of the ultrasonic system under actual cutting conditions.

Overall, the proposed approach offers a practical, cost-effective, and scalable solution for enhancing the performance of ultrasonic vibration-assisted milling processes.

Author Contributions: Conceptualization was proposed by T.-C.P. and N.-P.V., while all authors contributed to the discussion and refinement of the research concept. T.-C.P. carried out the experimental work and performed the analysis of the experimental data with the support of T.-Q.L. and H.-D.T. The manuscript was prepared and revised collaboratively by T.-C.P. and N.-P.V. All authors have read and agreed to the published version of the manuscript.

Funding: This research received no external funding.

Data Availability Statement: The original contributions presented in this study are included in the article. Further inquiries can be directed to the corresponding author.

Acknowledgments: This work was supported by Thai Nguyen University of Technology.

Conflicts of Interest: The authors declare no conflicts of interest.

Abbreviations

The following abbreviations are used in this manuscript:

MRR	Material removal rate
Ra	Surface roughness
NSGA-II	Non-dominated sorting genetic algorithm II
UVAM	Ultrasonic vibration-assisted machining
GPR	Gaussian process regression
RSM	Response surface methodology
IGD	Inverted generational distance

References

1. Han, G.; Wen, X.; Sun, J.; Ye, Z.; Wan, W.; Wang, Y.; Liu, F.; Bai, W.; Jiang, H. Finite element analysis and experimental study of longitudinal-torsional ultrasonic vibration-assisted milling of basalt fiber reinforced polymer composite. *Compos. Part A Appl. Sci. Manuf.* **2025**, *198*, 109166. [CrossRef]
2. Gao, P.; Wang, M.; Liang, Z.; Gao, X.; Zan, T. Surface morphology generation mechanism of cortical bone longitudinal-torsional ultrasonic vibration assisted micro-milling. *J. Manuf. Process.* **2025**, *145*, 300–312. [CrossRef]
3. Zhang, Y.; Ren, J.; Zhou, J. Effect of Ultrasonic Vibration-Assisted Milling on Surface Quality of Carbon Fiber Reinforced Polymer. *J. Mater. Res. Technol.* **2025**, *36*, 7373–7386. [CrossRef]
4. Xu, M.; Li, Y.; Xiang, D.; Song, C.; Yuan, Z.; Zhang, Z.; Yang, S.; Ma, M.; Gao, G.; Tong, J. Surface quality study of SiCp/Al composites by laser-ultrasonic vibration-assisted milling (LA-UVM). *Opt. Laser Technol.* **2025**, *188*, 113030. [CrossRef]
5. Zhang, M.; Yang, J.; Jiao, F.; Wang, X.; Liu, H.; Lv, Y. Mechanical force modeling and experimental verification of ultrasonic vibration assisted milling of high volume fraction SiCp/AL. *J. Alloys Compd.* **2025**, *1016*, 178870. [CrossRef]

6. Wang, J.; Chen, G.; Wang, S.; Hou, Y.; Xu, J.; Yu, H. Study on the removal behavior of constituent phases of SiCp/Al composites by ultrasonic vibration-assisted milling. *Mater. Today Commun.* **2025**, *42*, 111183. [CrossRef]
7. Gao, G.; Xiang, Y.; Qiao, H.; Wei, C.; Wang, G.; Xiang, D. Modeling on cutting force considering tool flank wear in ultrasonic vibration-assisted milling Ti3Al. *Wear* **2025**, *566*, 205761. [CrossRef]
8. Yan, T.; Zhu, L.; Shi, W.; Qin, S.; Chen, M.; Qin, Q. Cutting force prediction of longitudinal-torsional ultrasonic assisted milling based on synergistic prediction ensemble learning model: A case study on CFRP. *Compos. Part A Appl. Sci. Manuf.* **2025**, *190*, 108702. [CrossRef]
9. Zhang, C.; Qiu, Y.; Jiao, F.; Wang, J.; Wang, X. Research on temperature characteristics and the machining process in laser ultrasonic-assisted milling of cemented carbide. *Int. J. Refract. Met. Hard Mater.* **2025**, *128*, 107031. [CrossRef]
10. Xu, M.; Wei, R.; Cao, L.; Li, J.; Xiong, X.; Yu, L.; Li, C.; Ko, T.J. Cutting force modeling and machinability investigation of Inconel 718 using ultrasonic vibration-electrical discharge assisted milling. *J. Manuf. Process.* **2025**, *136*, 1–17. [CrossRef]
11. Ding, S.; Zhou, J.; Wang, B.; Guo, X.; Ren, Y.; Xu, Y. Ultrasonic vibration-assisted short electric arc milling of Inconel 718: Influence of electrode materials on surface integrity. *Mater. Today Commun.* **2025**, *44*, 111954. [CrossRef]
12. Zhang, G.; Yang, S.; Deng, Y.; Liang, C.; Song, T.; Wu, Y. Experimental study on surface finish and tool wear in ultrasonic vibration-assisted milling of nickel-based single-crystal superalloys. *Precis. Eng.* **2025**, *94*, 571–581. [CrossRef]
13. Wang, Z.; Chen, G.; Wang, J.; Jin, L.; Wu, Z.; Zhu, F. Variable direction shear deformation induced strengthening mechanism of Ti-6Al-4V alloy treated by a novel ultrasonic milling-burnishing process. *J. Manuf. Process.* **2025**, *144*, 294–310.
14. Sun, Z.; Liu, Y.; Geng, D.; Zhang, D.; Ying, E.; Liu, R.; Jiang, X. Cutting performance and surface integrity during rotary ultrasonic elliptical milling of cast Ni-based superalloy. *J. Mater. Res. Technol.* **2025**, *35*, 980–994. [CrossRef]
15. Teimouri, R.; Grabowski, M. Effect of ultrasonic vibration on fatigue life of Inconel 718 machined by high-speed milling: Physics-enhanced machine learning approach. *Mech. Syst. Signal Process.* **2025**, *224*, 112115.
16. Zhang, P.; Zhang, S.; Ge, S.; Jiang, X.; Chen, X. Study on the friction and wear properties of 7075-T6 aluminum alloy enhanced by milling and ultrasonic impact treatment. *Vacuum* **2024**, *230*, 113699. [CrossRef]
17. Dinh, V.-T.; Do, T.-T.; Le, T.-Q.; Luu, A.-T.; Vu, N.-P.; Tran, T.-P.-T. Initial Research on Ultrasonic Vibration-Assisted EDM for Processing Cylindrical Surfaces. *Coatings* **2025**, *15*, 463. [CrossRef]
18. Ha, T.-T.; Luu, A.-T.; Vu, N.-P. Multi-Objective Optimization of Surface Roughness and Material Removal Rate in Ultrasonic Vibration-Assisted CBN Grinding of External Cylindrical Surfaces. *Coatings* **2026**, *16*, 333. [CrossRef]
19. Ensminger, D.; Stulen, F.B. *Ultrasonics: Data, Equations and Their Practical Uses*; CRC Press: Boca Raton, FL, USA, 2008.
20. Brehl, D.A.; Dow, T. Review of vibration-assisted machining. *Precis. Eng.* **2008**, *32*, 153–172. [CrossRef]
21. Hung, L.X. Study on the Technological Conditions for Wheel Dressing, Lubrication–Cooling, and Determination of the Optimal Grinding Wheel Diameter During Wheel Replacement to Improve the Efficiency of Internal Grinding. Ph.D. Thesis, Thai Nguyen University of Technology, Thai Nguyen, Viet Nam, 2019.
22. Derks, P.L.L.M. The Design of Ultrasonic Resonators with Wide Output Cross-Sections. Ph.D. Thesis, Eindhoven University of Technology, Eindhoven, The Netherlands, 1984.